Understanding Slurry Formulations to Guide Solution-Processing of Solid Electrolytes

Anand Parejiya[a,b,*], Marm B. Dixit[a], Dhrupad Parikh[a], Ruhul Amin[a], Rachid Essehli[a], Jianlin Li[a], David L. Wood III[a], Ilias Belharouak[a,*]

a) Electrification and Energy Infrastructures Division, Oak Ridge National Laboratory, Oak Ridge, Tennessee 37831, United States

b) Bredesen Center for Interdisciplinary Research and Graduate Education, University of Tennessee, Knoxville, Tennessee 37996, United States

Corresponding authors*: Ilias Belharouak (belharouaki@ornl.gov)
Anand Parejiya (anandad111@gmail.com)

Authors emails: Marm B. Dixit (dixitmb@ornl.gov)
Dhrupad Parikh (parikhdhrupad@gmail.com)
Ruhul Amin (aminr@ornl.gov)
Rachid Essehli (essehlir@ornl.gov)
Jianlin Li (lij4@ornl.gov)
David L. Wood III (wooddl@ornl.gov)

Abstract

Scalable processing of thin solid electrolytes is crucial for engineering solid-state batteries with practical energy densities. To leverage existing battery production infrastructure, pathways for solution processing of solid electrolyte films must be investigated. Roll-to-roll compatible film preparation of aluminum-doped lithium lanthanum zirconate oxide was studied. Four slurry configurations accounting for different solvent properties and solid loadings were evaluated to investigate the ternary interactions within the dispersions. Rheological and coating stability analyses were carried out on the processed slurries. The analysis and characterization indicated that improved component interactions within the ethanol/toluene system result in homogenized distribution of the particles, binder, and plasticizer, and enable the extraction of free-standing thin films with thicknesses of 20 μm and large area (>15 $in.^2$). The drawbacks and opportunities of several protocols for high temperature sintering of the dried green films were investigated. This study highlights the importance of engineering dispersions during the development of processing protocols for solid electrolytes and provides guidelines for the best practices that can be leveraged for solution processing–based fabrications for a wide range of solid electrolyte materials.

Keywords

Roll to roll, Solid electrolyte, Slurries, Solid state batteries, Processing, Garnet

1. Introduction

To increase the adoption of electrified mobility alternatives, safe, high–energy density batteries must be developed [1,2]. Conventional lithium-ion batteries are not inherently safe because the liquid electrolyte contains flammable solvents [3]. Solid-state batteries (SSBs), which replace the liquid electrolyte with its solid counterpart, are theoretically safer because they do not contain flammable solvents [4–9]. Despite many efforts in material development, cell architecture optimizations, and processing inventions, SSBs have not yet been commercialized [10,11]. The US Department of Energy's performance and cost goals for electric vehicle batteries are energy density greater than 350 Wh kg^{-1} and costs lower than $60/kWh at the cell level [2,12]. These goals require the development of next-generation batteries with highly ionic conducting electrolytes and the use of energy-dense anodes and high-voltage, high-loading cathode materials. Use of lithium-metal anodes in conventional lithium-ion batteries is limited by various parameters such as safety and side reactions [13]. Furthermore, liquid electrolytes have narrow electrochemical stability windows, which hinder the use of high-voltage cathode materials [14]. However, a solid electrolyte (SE) allows the use of lithium metal because a dense SE can theoretically prevent dendrite formation [15,16], and many SEs have wide electrochemical stability windows, allowing integration of high-voltage cathode materials [3].

To develop a safe, energy-dense, and cost-effective battery, liquid electrolytes must be replaced by their solid counterparts [17–19]. Some challenges must be addressed concerning the ionic conductivity of SEs, chemical and electrochemical stability of anode | SE and cathode | SE, and the processability of SEs [10,20]. Many garnet SEs have ionic conductivity in the range of 10^{-4} to 10^{-3} S/cm and have a very wide electrochemical and chemical stability window [21–23]. Despite these favorable electrochemical, chemical, and transport properties, garnet-based SSBs have not been commercialized because garnets are brittle and have high Young's modulus with low fracture toughness [24]. These properties are not

favorable for attaining intimate contact between lithium-metal | SE and SE | cathode, and the solutions to these issues are not cost-effective, generally requiring additional processing steps and materials [25–28]. Furthermore, garnets have a higher density than other SEs, which adversely affects the gravimetric energy density when processed in currently employed form factors.

To enable garnet-based SE research, thick (1–2 mm) SEs are used at lab scale [11]. SE thickness is a critical parameter that enables garnet-like, high-density SEs to achieve gravimetric energy-density metrics relevant to electric vehicle applications [29,30]. Currently, average lithium, SE, and cathode thicknesses used in all-solid-state batteries are 100, 500, and 30 µm, respectively[11]. The energy density metrics for cells with such thicknesses are lower than those of conventional lithium-ion batteries (approximately 10–100 Wh kg^{-1}). Furthermore, SSBs are cycled at very high pressures in the range of approximately 10 MPa to obtain intimate contact between solid–solid interfaces in the SSB (anode | SE and cathode | SE) [31,32]. The brittle nature of garnets limits the maximum allowable pressure on the cell. Transitioning to a thin SE film can mitigate these issues by decreasing the overall material cost, providing facile mechanical properties for ease of handling, and reducing the ion transport path to enable fast charging capabilities of the battery. Thus, developing strategies to manufacture thin, dense-defect–free SEs at scale is necessary for a successful deployment of SSBs in electric vehicles. However, efforts to address this challenge are not well documented [10,30]. A thin and very dense layer of electrolyte may be created via physical vapor deposition or atomic layer deposition, but these methods pose concerns of scalability and costs associated with large-scale production [33]. Tape casting, or roll-to-roll processing, is the most promising technology for manufacturing thin, dense-defect–free SEs SE sheets. Roll-to-roll processing of SEs can also use the existing infrastructure for conventional lithium-ion battery manufacturing for successful deployment of SSBs [34].

Significant challenges must be overcome to facilitate slurry processing for making thin, dense electrolytes. This process is illustrated in Figure 1. The structure and properties of roll-to-roll–coated SEs are a function

of the interactions that occur among the constituents in the dispersion. Slurry processing involves coating, drying, calendering, delaminating, and sintering electrolyte films at high temperatures to eliminate solvent-binder-plasticizer systems. These systems affect the lithium lanthanum zirconate oxide (LLZO) properties, including microstructure, density, hardness, shrinkage, and conductivity. Significant work has been devoted to slurry engineering for electrodes in fuel-cell technologies and conventional lithium-ion batteries [30,35–40]. In this study, the underlying principles of ternary component interactions in the dispersions were leveraged to achieve roll-to-roll coatings of free-standing aluminum-doped lithium lanthanum zirconate oxide (LALZO) SE films. The slurry composition of the solvent-binder-plasticizer system was optimized to form a defect-free green tape that can be delaminated to obtain free-standing LLZO thin films. Various sintering strategies were evaluated to obtain a flat, dense-defect–free SE film. Lithium loss was optimized in the SE densification to achieve a homogeneous composition of LLZO. Experimental strategies and best practices for solution processing of SEs can also be leveraged for other SEs.

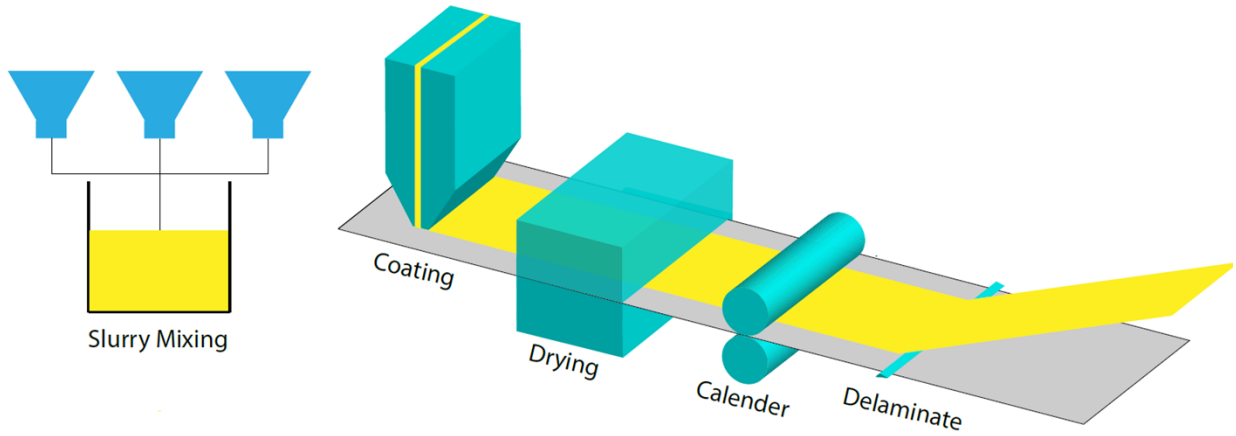

Figure 1. The steps for solution processing of SEs. (left) The first step is to obtain a homogenized dispersion of components within a solvent using appropriate mixing strategies. (right) Next, this slurry is casted using a slot-die coating and undergoes several stages of postprocessing to obtain dried, free-standing green films.

2. Experimental

2.1. Slurry Preparation

Commercial LALZO was used for this study. Slurries were prepared using two solvent systems: (1) isopropyl alcohol (IPA) and toluene and (2) ethanol and toluene. Fish oil was used as a dispersant, benzyl butyl phthalate was used as a plasticizer, and polyvinyl butyral (PVB) was used as a binder. Yttrium-stabilized zirconium balls were used as a milling media. Four slurries were prepared using the compositions listed in Table 1. The constituents were mixed in specific ratios and ball milled in a spex mill for 1 h followed by degassing under vacuum for 10 min.

Table 1. Composition of the four slurries used in this study

Component	Slurry 1 (wt. %)	Slurry 2 (wt. %)	Slurry 3 (wt. %)	Slurry 4 (wt. %)
LALZO	25	37	25	37
IPA	21	15	0	0
Ethanol	0	0	21	15
Toluene	21	15	21	15
Fish oil	0.5	0.5	0.5	0.5
Yttrium-stabilized zirconium	22.5	22.5	22.5	22.5
Benzyl butyl phthalate	5	5	5	5
PVB	5	5	5	5

2.2. Rheology

After degassing, the slurries were transferred to the rheometer (Discovery HR-3, TA Instruments). A SmartSwap concentric cylinder geometry (bob diameter = 28.05 mm, bob length = 42.01 mm) was used

for the rheological measurements. The slurries presheared at 5 rad s^{-1} for 10 s followed by an equilibration step of 15 min. Then a flow ramp test was performed from shear rates of 5 to 3,500 s^{-1} to measure the shear-dependent viscosity.

2.3. Tape Casting

For tape casting, the slurries were used immediately after the mixing step and subsequent degassing. The slurries were tape cast on the shiny side of mylar sheets on a benchtop coater. Rheology and coatings were carried out on separate slurry samples. The coating speed for all the coatings was maintained at 40 mm/s. The coatings were dried at room temperature for 24 h in a dry room. Wet thicknesses of 50, 100, 150 and 200 µm were cast on the mylar substrate for all the slurries. After extensive drying, the coatings were delaminated from the mylar substrates.

2.4. Densification

After delamination, the dry coatings were punched and then underwent three annealing steps. The first annealing was carried out in an argon environment in a tube furnace at 600°C for 12 h to remove the binder-plasticizer-dispersant. The second annealing was carried out at 1,100°C for 12 h in an argon environment for densification of the films. Four substrate systems were analyzed for densification of LALZO thin sheets: (1) green films buried in LALZO mother powder on an alumina crucible, (2) bare green film on alumina crucible, (3) green film sandwiched between two alumina crucibles, and (4) green film sandwiched between graphite sheets that are sandwiched between alumina sheets. The dense pellets of the fourth substrate system underwent a third annealing in a box furnace in air at 500°C for 2 h to remove the carbon contamination from the surface.

2.5. Material Characterization

The microstructures of the dried green films and sintered sheets were analyzed via scanning electron microscopy (SEM) using a Zeiss MERLIN FE-SEM. All SEM micrographs were collected at 1 kV electron high

tension and a working distance of 5.5 mm. X-ray diffraction (XRD) measurements were performed using Panalytical Xpert Pro at 45 kV and 40 mA conditions. The XRD data were collected at room temperature in the range of 15° to 60° with a step size of 0.01° using Cu-Kα radiation.

3. Coating Stability Window Model

The stability windows for slot-die coatings of non-Newtonian slurries are well documented [41–47]. The model used for predicting coating stability windows is briefly described as follows. A full derivation of the model can be found elsewhere [41–47]. Figure 2 shows a diagram of fluid flow through a slot die coater with key elements of the flow profile identified. A uniform coating window is specified in terms of the fluid flow parameters for the coating bead shown in Figure 2. The coating bead has a free boundary that wets the web (upstream meniscus), and the downstream free surface is identified by the film-forming meniscus (downstream meniscus). The relevant physical parameters of interest in this case are the coating speed u_w, the gap height h_G, the upstream lip length l_u, the downstream lip length l_d, and the wet film height h. The flow parameters of the slurry—viscosity η, flow behavior index ϵ, and surface tension σ—also affect the coating stability. Generally, the 3D flow problem is simplified into a 2D or 1D problem (in the gap) to aid analysis. The stability of the coating window is determined by the position and nature of the upstream meniscus and is classified into four cases: (1) corresponding to the a concave upstream meniscus pinned to the end of the upstream lip, (2) corresponding to a convex meniscus pinned to the end of the upstream lip, (3) corresponding to a concave upstream meniscus pinned to the lower end of the upstream lip, and (4) corresponding to a convex upstream meniscus pinned to the lower end of the upstream lip. The individual pressure drops for each case for a non-Newtonian fluid are given as follows:

$$\Delta P_{DU,\,case\,1} = \left[-l_D k \left(\frac{(\epsilon+1)(2\epsilon+1)}{\epsilon} \right)^{\epsilon} \left(\frac{(h_G - 2h)^{\epsilon}}{h_G^{(2\epsilon+1)}} \right) u_w^{\epsilon} \right] + \left[l_U k \left(\frac{(\epsilon+1)(2\epsilon+1)}{\epsilon} \right)^{\epsilon} h_G^{-(\epsilon+1)} u_w^{\epsilon} \right] + 1.34 \left(k \frac{u_w^{\epsilon}}{\sigma h_G^{(\epsilon+1)}} \right)^{\frac{2}{3}} \frac{\sigma}{h} + \frac{2\sigma}{h} \quad (1)$$

$$\Delta P_{DU,\,case\,2} = \left[-l_D k \left(\frac{(\epsilon+1)(2\epsilon+1)}{\epsilon} \right)^{\epsilon} \left(\frac{(h_G - 2h)^{\epsilon}}{h_G^{(2\epsilon+1)}} \right) u_w^{\epsilon} \right] + \left[l_U k \left(\frac{(\epsilon+1)(2\epsilon+1)}{\epsilon} \right)^{\epsilon} h_G^{-(\epsilon+1)} u_w^{\epsilon} \right] + 1.34 \left(k \frac{u_w^{\epsilon}}{\sigma h_G^{(\epsilon+1)}} \right)^{\frac{2}{3}} \frac{\sigma}{h} - \frac{2\sigma}{h} \quad (2)$$

$$\Delta P_{DU,\,case\,3} = \left[-l_D k \left(\frac{(\epsilon+1)(2\epsilon+1)}{\epsilon} \right)^{\epsilon} \left(\frac{(h_G - 2h)^{\epsilon}}{h_G^{(2\epsilon+1)}} \right) u_w^{\epsilon} \right] + 1.34 \left(k \frac{u_w^{\epsilon}}{\sigma h_G^{(\epsilon+1)}} \right)^{\frac{2}{3}} \frac{\sigma}{h} + \frac{2\sigma}{h} \quad (3)$$

$$\Delta P_{DU,\,case\,4} = \left[-l_D k \left(\frac{(\epsilon+1)(2\epsilon+1)}{\epsilon} \right)^{\epsilon} \left(\frac{(h_G - 2h)^{\epsilon}}{h_G^{(2\epsilon+1)}} \right) u_w^{\epsilon} \right] + 1.34 \left(k \frac{u_w^{\epsilon}}{\sigma h_G^{(\epsilon+1)}} \right)^{\frac{2}{3}} \frac{\sigma}{h} - \frac{2\sigma}{h} \quad (4)$$

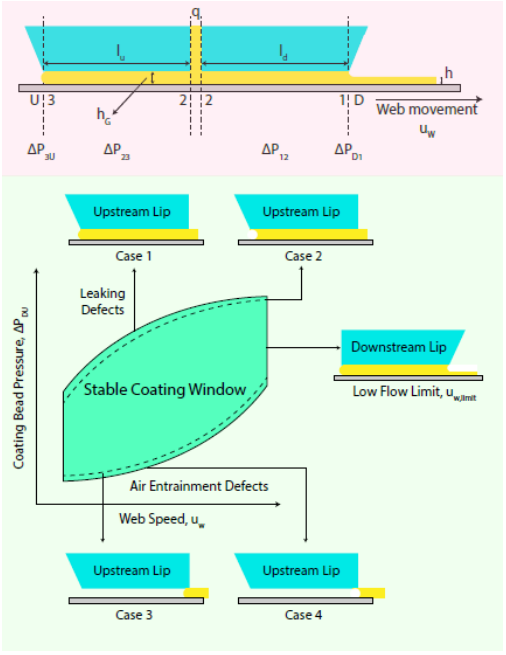

Figure 2. Cross-sectional view of the slot-die coater near the moving web. Coating stability windows with respect to coating bead pressure and the web speed are highlighted, along with the defect routes. Cases 1–4 denote the positions of the upstream meniscus that are used to assess the coating stability windows.

4. Results and Discussion

The development of successful roll-to-roll processing for SEs requires the engineering of stable, functional dispersions. Dispersion stability is a key requirement for achieving high-quality coatings and improving the shelf life of the slurry [36]. Dispersion stability is dictated by the competing interactions between the solvent, dispersed particles, binders, and surfactant. These interactions typically include van Der Waals, electrostatic, steric, and depletion interactions [48–51]. Two distinct solvent systems and loading configurations were investigated to evaluate the relative interactions and their influence on LLZO coatings. Four slurry configurations were prepared, as described in Table 1. The differences in these solvent properties allow effective investigation of the influence of various interactions and provide insight into best practices for slurry preparation for LALZO coatings. Visual analyses of the dispersion stability and quality did not indicate any aggregations within any of the slurries, which suggests that the components were homogenized by the high-energy ball milling. However, the ethanol slurry dried quickly, which limited the time available to create coatings. The vapor pressure of IPA is 4.1 kPa, and the vapor pressure of ethanol is 5.95 kPa at 25 °C; thus, ethanol has a faster evaporation rate than IPA[30,36]. In the dry room environment where these slurries were processed and casted, the processing window of an exposed IPA-based slurry was approximately 15–20 min, whereas dried aggregates could be observed in an exposed ethanol-based slurry after only a few minutes. Furthermore, the lower total solvent content in the slurries with higher solid loading caused them to be less stable than the slurries with lower solid loading[52]. Depending on the humidity levels, these stability values might change significantly, but solvent content does affect processing timescales and shelf life.

Rheological measurements of the slurry were performed to assess the shear-dependent viscosity of the slurries. Newtonian slurries are preferred because they enable wide coating windows and defect-free coatings [53]. However, most practical multicomponent dispersions used for batteries exhibit shear-

thinning behavior [54]. This behavior arises from the breakup of large agglomerate structures within the dispersions upon application of high shear rates. Shear-thinning fluids are defined by the power law model for viscosity given as $\tau = \mu\dot{\gamma}^{\in-1}$, where τ is the shear stress, μ is the flow consistency index, and ϵ is the flow behavior index [41,55]. For shear-thinning fluids, $\in$ is less than unity. The shear-dependent viscosities for the investigated slurries are shown in Figure 3. The IPA/toluene slurry shows Newtonian behavior for a large shear-rate window followed by shear thinning. In contrast, the ethanol/toluene slurry shows a near shear thinning behavior for the entire range of shear rates involved. Both the IPA/toluene slurries have higher viscosity than the ethanol toluene slurry for the same loading. Viscosity of the dispersions is dictated by the component interactions within it: polymer–solvent, polymer–particle, and particle–solvent. As mentioned previously, the interactions between the constituents of dispersions are van Der Waals attraction, electrostatic repulsion, depletion/bridging interaction, or steric repulsion. IPA has a dielectric constant of 17.9, ethanol has a dielectric constant of 24.5, and toluene has a dielectric constant of 2.38. The differences in electrostatic interactions within the dispersions are completely dictated by the polarization capability of the alcohol component, which is higher in ethanol compared to IPA [56–58]. A higher polarization capability leads to fewer interactions between the components. Ethanol also has a slightly higher surface tension (22.4 mN/m) than IPA (21.3 mN/m), which indicates a higher Hamaker constant, resulting in higher van Der Waals attraction [50,59]. However, this force is typically short-ranged, and the slurry interactions at the present configurations were dominated by electrostatics and polymer-based interactions. Another key factor dictating dispersion viscosity is the behavior of the polymer in the solvent system. The dispersion (δ_D), polar (δ_P), and hydrogen (δ_H) bonding contributions and the total solubility parameter (δ) are listed in Table 2 [60]. These components depict the energy density of the specified interaction (dispersion bonds, intermolecular forces, hydrogen bonding respectively) for the components. To enable effective dispersions, similar solubility parameters between the dispersed material and solvent should be maintained [36,60–62]. Therefore, PVB should be more

compatible with the IPA/toluene ink than with the ethanol/toluene slurries. This compatibility would result in the IPA/toluene slurries having a better interaction among the polymer, solvent, and particle. This interaction yields the higher viscosities observed for the IPA/toluene slurries compared with the ethanol/toluene slurries. Furthermore, higher solid loading increases the overall viscosity across the range of the investigated shear rates. The flow profiles were fit to the power law model, and the consistency index and flow behavior index are given in Table 3. The IPA/toluene slurries have a higher flow consistency index and lower flow behavior index than the ethanol/toluene slurries. Shear rates for roll-to-roll coatings are typically dictated by the coating height (h_w) and coating speed (u_w) and are given as the ratio of the coating height to coating speed. Figure 3 shows the shear rates experienced on the slurry at 40 mm/s coating speed with wet height thicknesses of 50, 100, and 150 µm. As the wet coating height increases, the shear rate experienced by the slurry decreases.

Table 2. Solubility parameters for each solvent

Solvent	Dispersion bonding contribution, δ_D ($MPa^{1/2}$)	Polar bonding contribution, δ_P ($MPa^{1/2}$)	Hydrogen bonding contribution, δ_H ($MPa^{1/2}$)	Total solubility parameter, δ ($MPa^{1/2}$)
PVB	7.72	2.90	3.26	8.87
Ethanol	15.8	8.8	19.4	26.0
Toluene	18.0	1.4	2.0	18.3
IPA	15.8	6.1	16.4	23.8

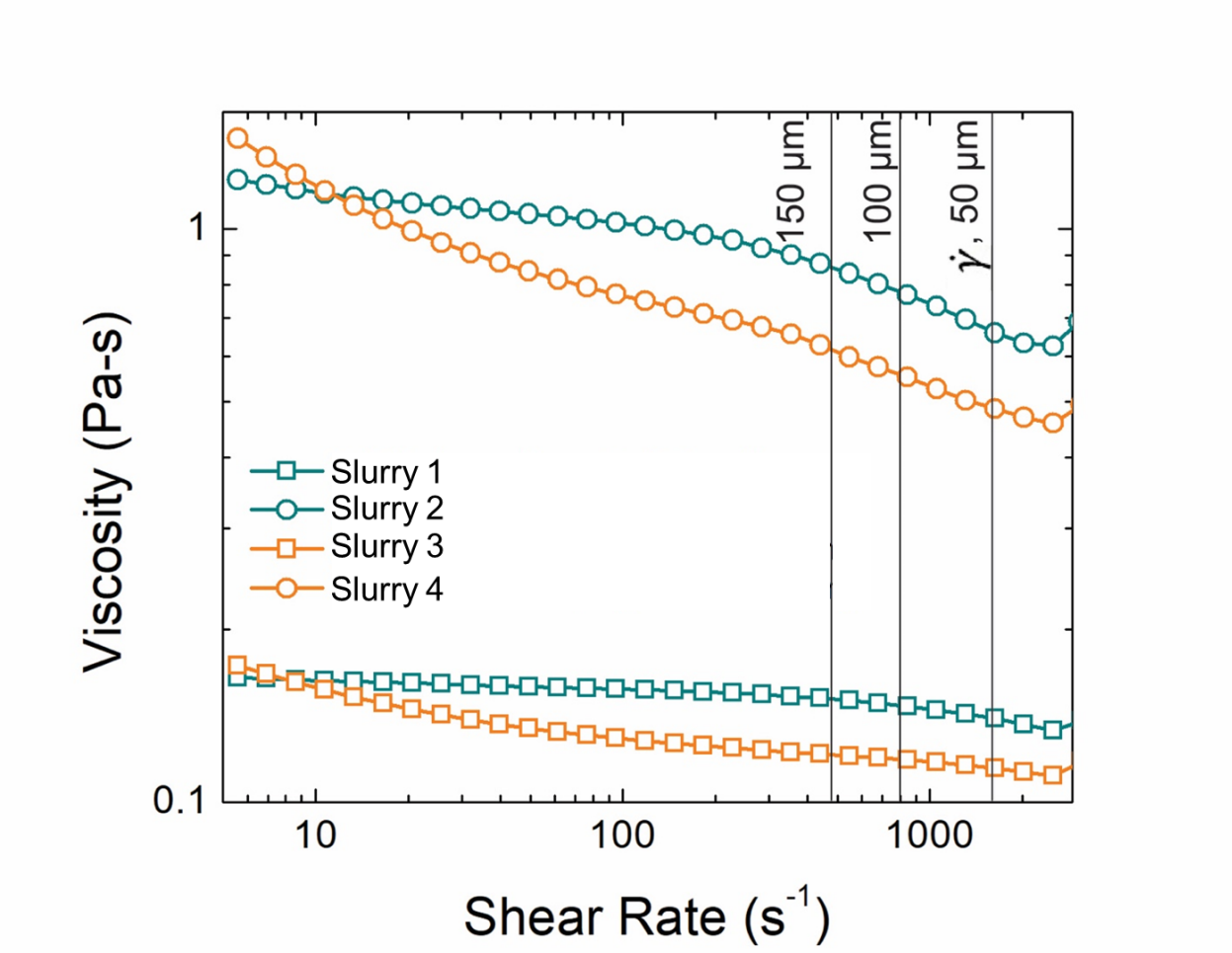

Figure 3. Shear sweeps for the four slurries performed using a DHR-3 rheometer. All slurries were presheared and equilibrated prior to measurement of the shear sweeps. Relevant shear rates for processing wet height thicknesses of 50, 100, and 150 µm at 40 mm/s are denoted by vertical lines.

The rheological properties of the slurry significantly affect the thickness of the coated layer and the morphology of the electrode during and after drying [40]. The rheological properties also dictate the available coating windows and processing parameters. The models for assessing coating windows from rheological information are well established and are governed by the viscocapillary forces acting within the slot-die head [41,43,55,63]. Coating windows are defined by the coating speeds and the maximum allowable pressure drop across the slot die. Depending on the position of the upstream and downstream menisci, leaking defects, low-flow limit, and air entrainment defects can be observed, as shown in Figure 2.

In ideal coating conditions, the upstream meniscus is pinned to the farther edge of the slot-die lip. Leaking defects occur if the fluid pressure exceeds the pressure drop across the lip and cause an uncontrolled coating width. No upstream meniscus is present in this case, and the slurry spreads out of the slot die. This situation can lead to significant material losses and contamination of the processing instruments. The low flow limit occurs at high coating speeds at which the fluid pressure is not sufficient to maintain the desired wet thickness. The downstream meniscus shifts such that the coating height is not maintained at the exit of the slot die. In these conditions, the resultant coatings will be of nonuniform thickness, which can have detrimental effects on the subsequent processing and integration steps. Finally, the air entrainment defect is an exacerbated case of the low flow limit in which the fluid pressure drops low enough for the upstream meniscus to travel all the way to inner edge of the upstream lip and allow air to be integrated into the coated fluid. This results in intermittent coatings with less control over the coating thicknesses.

The coating windows for the formulated slurries were investigated using the Eqs. 1–4 for non-Newtonian fluids using the fits obtained by the power law model (Table 3). Figure 4 shows the effects of processing parameters on operating window for the four investigated LALZO slurries. The IPA/toluene slurry offered a wider coating window compared with the ethanol/toluene counterparts. Furthermore, the slurries with higher solid loadings resulted in wider coating windows in terms of pressure compared with those with low solid loadings, and the less viscous systems were favorable for high-speed operations (web speeds >10 m/min). This behavior was expected because lower viscosities and slurry densities tend to minimize the available range of operation in terms of fluid pressure before running to leaking and air entrainment effects. However, ease of flow minimizes the chance of hitting the low flow limits for these systems. The higher-viscosity slurries would have higher pumping requirements (watts per liter pumped) compared with the slurries with lower loading. Designing processes for scalable manufacturing of SEs requires careful tuning of the slurry rheology because it dictates the quality of the coatings, the processing

conditions, the control requirements, and the process flexibility. Higher loadings are preferred for relatively slower coating lines, which require flexibility in terms of operation and less accurate controls. Lower loadings are preferred for high-speed coating lines with highly accurate controls, which result in limited processing flexibility but high throughputs.

Table 3. Slurry rheological and gravimetric metrics

Slurry	Flow consistency index	Flow Behavior index	Slurry density (g cm^{-3})
Slurry 1	0.237	0.928	1.188
Slurry 2	3.012	0.79	1.464
Slurry 3	0.162	0.952	1.190
Slurry 4	1.79	0.821	1.466

The dried coated films prepared by the four slurries were subsequently investigated. SEM micrographs of all four dried slurries are shown in Figure 5(a–d). The micrographs are top-down views of the coatings with 50 µm wet thickness after drying. As shown in the figure, all four dry films show distinct morphology and particle distribution. After drying, slurries 1 and 2 had uniform LALZO particle distributions and uniform distributions of binder-plasticizer within the system. In contrast, aggregates of white particles (LLZO) were clearly observed for the ethanol-based slurries, which indicated a poor coating.

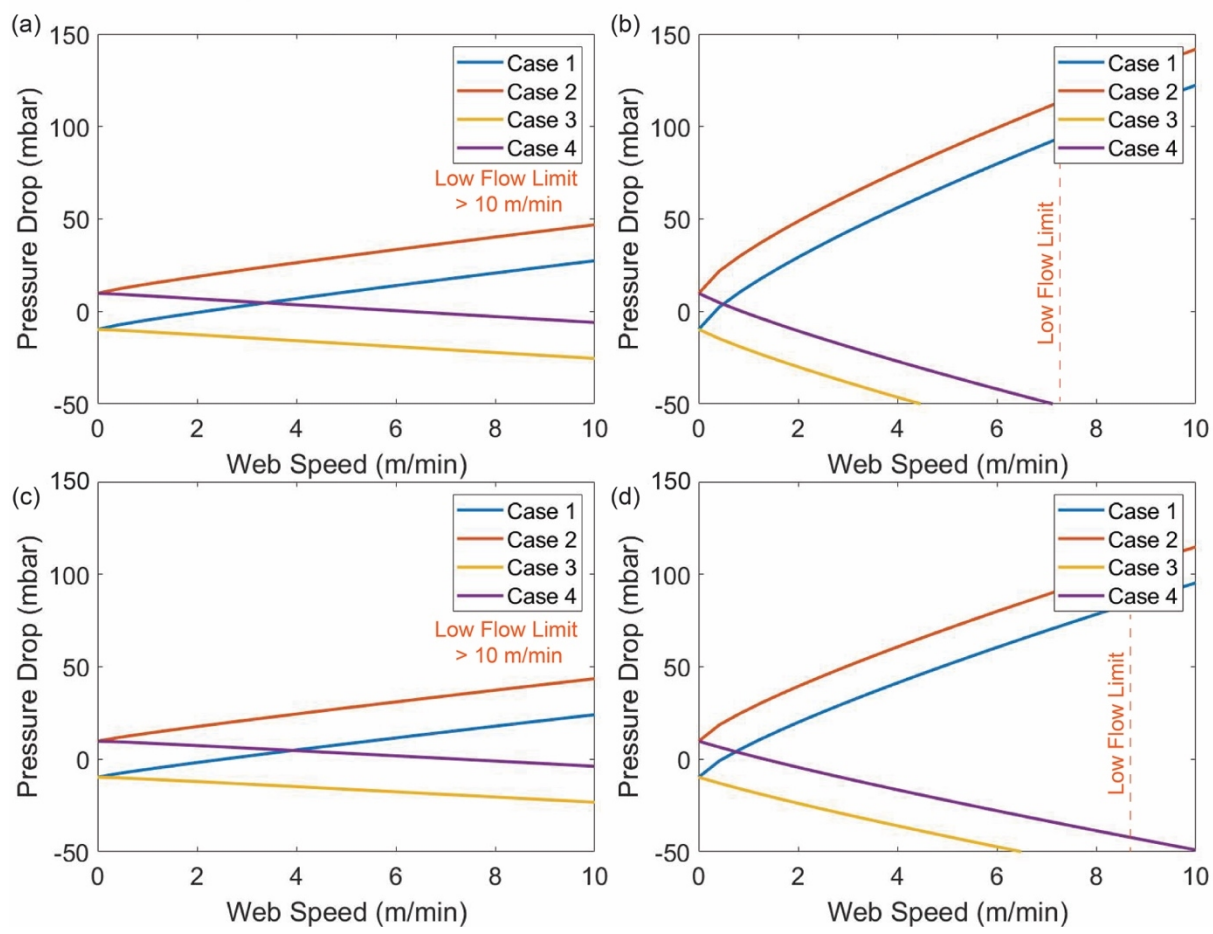

Figure 3. Effect of processing parameters on operating window for the investigated LALZO slurries: (a) ethanol/toluene low solid loading, (b) ethanol/toluene high solid loading, (c) IPA/toluene low solid loading, (d) IPA/toluene high solid loading. The low flow limit condition is identified for all the investigated slurries. Cases 1–4 in the legends represent the pressure drop for the four positions of the upstream meniscus detailed in Figure 2.

The porosity distribution was unique to all the slurries. After drying, more pores were visible in slurry 1 than in slurry 2 because of the different LALZO loading in the slurries. Higher LALZO loading results in fewer pores, which is desirable.

To achieve a dense, defect-free SE film, the green film must have a uniform particle distribution with high packing density. This configuration will facilitate lower-temperature annealing in less time because less particle growth is required during annealing compared with that for low–packing fraction green films. The

morphology and distribution behavior observed in the ethanol-based slurries is highly undesirable because it affects the delamination and densification.

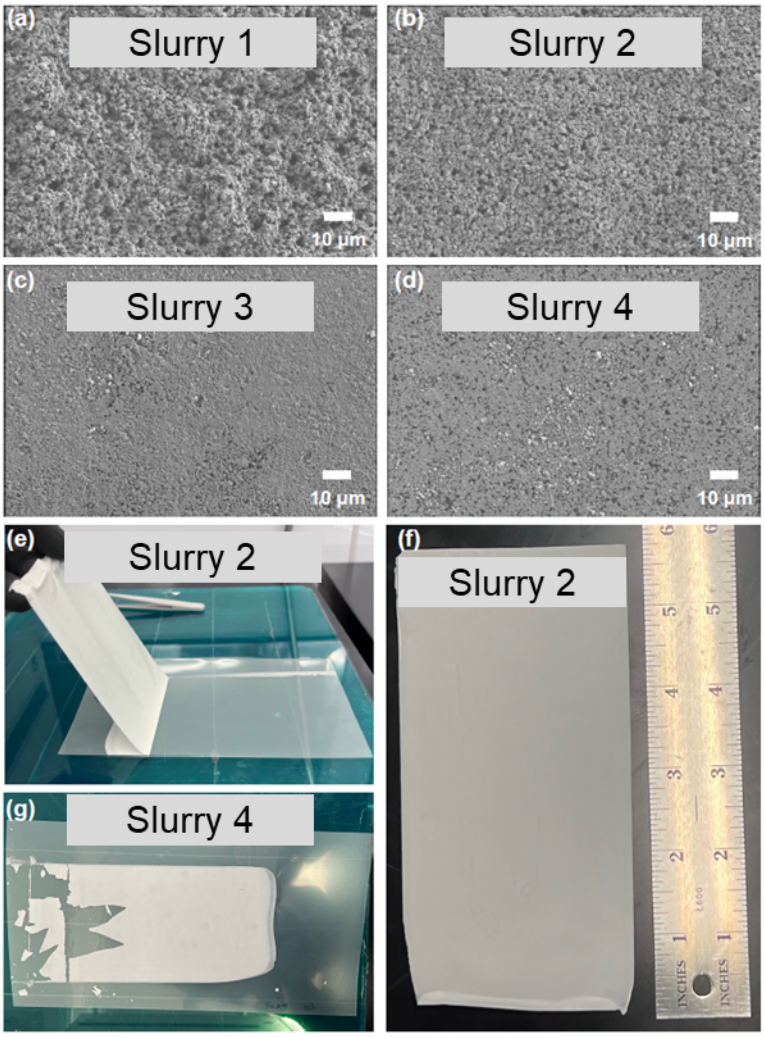

Figure 4. (a–d) SEM micrographs of the dried green films processed with IPA/toluene and ethanol/toluene slurries at low and high loadings. (e) Peel-off condition and (f) free-standing LALZO film obtained from the IPA/toluene slurries. The coated film can be separated from the mylar substrate in a single step with no defect generation. (g) Peel-off condition of the LALZO film processed with ethanol/toluene slurries. These coatings are brittle, and free-standing films cannot be separated from the mylar substrate.

Increase in annealing temperature and time can also lead to heterogenous chemical composition of the dense SE sheet because of elevated lithium loss and reduced formation energy of side products. The SEM micrographs reveal that slurries 1 and 2 yielded desirable microstructure of the green film. Integrating SEs into the SSB architecture would ideally require calendering of three individual, free-standing layers for the

cathode, separator, and the anode. Although the cathode and anode entities can be based on a backing/current collector, a free-standing separator film is required to integrate the SSB architectures. The ability of the coated systems to be manually peeled for creating free-standing thin films was investigated. As shown in Figure 5, all the slurries were peeled off manually. The coatings with the IPA/toluene slurry were easy to handle and led to extremely facile delamination from the mylar substrate. A free-standing green film with an area of 15 $in.^2$ and approximately 20 μm thickness could be delaminated directly from the coated substrate without any additional treatment, which is a significant step toward achieving roll-to-roll fabrication of LALZO thin films. In contrast, the coatings with ethanol/toluene as solvents did not delaminate effectively. Poor microstructural distribution and lack of uniformity of the binder-surfactant network caused decreased integrity of these films.

The final stage of the LALZO thin film preparation is densification, in which the coated thin films are sintered at high temperatures. We evaluated several pathways for effective sintering of the LLZO thin films as described qualitatively in Fig. 6a. Initially, an approach like pellet sintering was pursued: the green films were buried under excess mother powder to achieve high density and mitigate lithium loss. The resultant films had a wavy structure that prohibited their use in subsequent cell assembly because of the risk of fracture. Sintering without the mother powder also caused a wavy structure. In addition to this, this resulted in films with Li-loss as discussed below. We propose that nonuniform heating and densification might be the cause of the wavy structure. To minimize the waviness of the structure, sintering the green films between alumina plates was investigated. This approach was also not successful because the resultant films were brittle and adhered to the alumina plates, which subsequently fractured. Finally, sintering between graphite plates was investigated to minimize the potential diffusion between the green film and the backing plates. This resulted in flat sintered films, that were mechanically robust

and could be handled without breaking. Apart from the mechanical stability, phase stability and lithium loss of the sintered films was also investigated through XRD analysis.

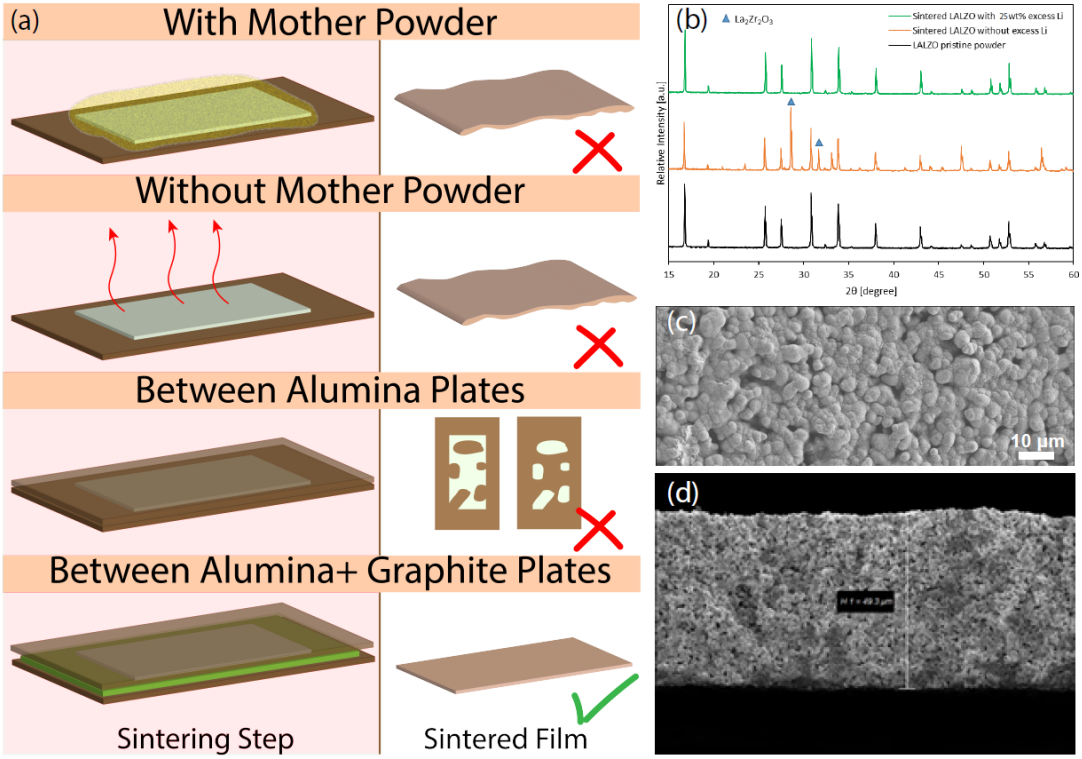

Figure 5. (a) Diagram of the approaches undertaken to carry out the densification sintering of the solution-processed green films, highlighting the approaches that failed and the approach that worked. (b) XRD patterns for the mother powder and the sintered films with optimized quantity of excess lithium. (c) Top view and (d) cross-sectional SEM images for the densified LLZO green film.

Phase quantification was carried out using GSAS software. A sharp $La_2Zr_3O_7$ peak is observed in the sintered garnet film when zero excess Li is added to the slurry (Fig. 6b). To mitigate this Li-loss, excess LiOH was added to the slurry. Green films prepared with this excess LiOH, when sintered between graphite plates, resulted in dense LLZO thin films. SEM micrographs of these densified films are shown in Figure 6c and 6d. These images show that the density of the sintered films is very high, and very small pores are present. We have estimated that the density of the sintered film is >90% with pore sizes in the order of 1-2 µm. Further we also observe that the sintered films shrunk ~60% compared to the unsintered green film. It should be noted that the mechanical properties of the resultant films are a crucial aspect of both

processing and performance of the solid-state batteries. As such, the unsintered green films can be wound and “rolled” in the traditional sense of the R2R processing. Due to the area constraints with our furnaces, we were only able to investigate the sintering performances of smaller pieces of the green films whose handling is discussed. In addition, the inherent mechanical properties of LLZO in general for films made with either solvent system would be similar. Electrochemical testing of sintered thin films requires careful experimental setup development for material handling which is beyond the scope of the present discussion. We establish that employing a graphite and alumina plate leads to improved structural integrity of the sintered films and their handling is improved. Sintering steps for roll-to-roll coating must consider compatible supporting plates and applications of pressure to maintain the form factor.

5. Conclusion

Scalable processing of thin SEs is crucial for the development of high–energy density SSBs. Factors that affect the slurry-based processing of LALZO-based thin films were investigated. Specifically, IPA/toluene and ethanol/toluene slurries at different solid loadings were used to investigate the influence of component interaction in the dispersion phase on the resulting film microstructure and processability. Improved component interactions within the IPA/toluene slurries yielded well-dispersed, homogenous microstructures. Furthermore, rheological investigations provided insight into the processing windows for roll-to-roll processing of the SEs. Several strategies were employed to densify the solution-processed green films and highlight the shortcomings and effectiveness of the approaches involved. These strategies can be effectively translated to other solid electrolyte materials, and they offer guidelines regarding the best practices for solution processing–based fabrications for solid electrolytes.

6. Acknowledgements

This research at Oak Ridge National Laboratory, managed by UT Battelle, LLC, for the US Department of Energy (DOE) under contract DE-AC05-00OR22725, was sponsored by Laboratory Directed Research and Development (LDRD) Program at Oak Ridge National Laboratory, and the Office of Energy Efficiency and Renewable Energy (EERE) Vehicle Technologies Office (VTO) (Deputy Director: David Howell) Applied Battery Research subprogram (Program Manager: Peter Faguy). Marm Dixit is supported by the Alvin M. Weinberg Fellowship at Oak Ridge National Laboratory.

7. References

[1] Z.A. Needell, J. McNerney, M.T. Chang, J.E. Trancik, Potential for widespread electrification of personal vehicle travel in the United States, Nat. Energy. 1 (2016). https://doi.org/10.1038/nenergy.2016.112.

[2] T.T. Mai, P. Jadun, J.S. Logan, C.A. McMillan, M. Muratori, D.C. Steinberg, L.J. Vimmerstedt, B. Haley, R. Jones, B. Nelson, Electrification Futures Study: Scenarios of Electric Technology Adoption and Power Consumption for the United States, Natl. Renew. Energy Lab. (2018) 151. https://doi.org/10.2172/1459351.

[3] Z. Gao, H. Sun, L. Fu, F. Ye, Y. Zhang, W. Luo, Y. Huang, Promises, Challenges, and Recent Progress of Inorganic Solid-State Electrolytes for All-Solid-State Lithium Batteries, Adv. Mater. 30 (2018) 1–27. https://doi.org/10.1002/adma.201705702.

[4] M.B. Dixit, A. Parejiya, N. Muralidharan, R. Essehli, R. Amin, I. Belharouak, Understanding Implications of Cathode Architecture on Energy Density of Solid-State Batteries, Energy Storage Mater. 40 (2021) 239–249. https://doi.org/https://doi.org/10.1016/j.ensm.2021.05.001.

[5] M. Dixit, N. Muralidharan, A. Parejiya, R. Amin, R. Essehli, I. Belharouak, Current Status and

Prospects of Solid-State Batteries as the Future of Energy Storage, in: Energy Storage Devices, IntechOpen, 2021.

[6] M.B. Dixit, J. Park, P. Kenesei, K.B. Hatzell, Status and prospect of in situ and operando characterization of solid-state batteries, Energy Environ. Sci. 14 (2021) 4672–4711. https://doi.org/10.1039/d1ee00638j.

[7] P. Albertus, V. Anandan, C. Ban, N. Balsara, I. Belharouak, J. Buettner-Garrett, Z. Chen, C. Daniel, M. Doeff, N.J. Dudney, B. Dunn, S.J. Harris, S. Herle, E. Herbert, S. Kalnaus, J.A. Libera, D. Lu, S. Martin, B.D. McCloskey, M.T. McDowell, Y.S. Meng, J. Nanda, J. Sakamoto, E.C. Self, S. Tepavcevic, E. Wachsman, C. Wang, A.S. Westover, J. Xiao, T. Yersak, Challenges for and Pathways toward Li-Metal-Based All-Solid-State Batteries, ACS Energy Lett. 6 (2021) 1399–1404. https://doi.org/10.1021/acsenergylett.1c00445.

[8] K.B. Hatzell, X.C. Chen, C. Cobb, N.P. Dasgupta, M.B. Dixit, L.E. Marbella, M.T. McDowell, P. Mukherjee, A. Verma, V. Viswanathan, A. Westover, W.G. Zeier, Challenges in lithium metal anodes for solid state batteries, ACS Energy Lett. 5 (2020) 922–934. https://doi.org/10.1021/acsenergylett.9b02668.

[9] J. Janek, W.G. Zeier, A solid future for battery development, Nat. Energy. 1 (2016) 16141. https://doi.org/10.1038/nenergy.2016.141.

[10] K. Kerman, A. Luntz, V. Viswanathan, Y.-M. Chiang, Z. Chen, Review—Practical Challenges Hindering the Development of Solid State Li Ion Batteries, J. Electrochem. Soc. 164 (2017) A1731–A1744. https://doi.org/10.1149/2.1571707jes.

[11] S. Randau, D.A. Weber, O. Kötz, R. Koerver, P. Braun, A. Weber, E. Ivers-Tiffée, T. Adermann, J. Kulisch, W.G. Zeier, F.H. Richter, J. Janek, Benchmarking the performance of all-solid-state lithium

batteries, Nat. Energy. 5 (2020) 259–270. https://doi.org/10.1038/s41560-020-0565-1.

[12] Steven Boyd, Batteries and Electrification R&D Overview, 2018. https://www.energy.gov/sites/prod/files/2018/06/f53/bat918_boyd_2018.pdf.

[13] K.N. Wood, M. Noked, N.P. Dasgupta, Lithium metal anodes: Toward an improved understanding of coupled morphological, electrochemical, and mechanical behavior, ACS Energy Lett. 2 (2017) 664–672. https://doi.org/10.1021/acsenergylett.6b00650.

[14] N.E. Galushkin, N.N. Yazvinskaya, D.N. Galushkin, Mechanism of Gases Generation during Lithium-Ion Batteries Cycling, J. Electrochem. Soc. 166 (2019) A897–A908. https://doi.org/10.1149/2.0041906jes.

[15] C. Monroe, J. Newman, Dendrite Growth in Lithium/Polymer Systems A Propagation Model for Liquid Electrolytes Under Galvanostatic Conditions, J. Electrochem. Soc. 150 (2003) A1377–A1384.

[16] C. Monroe, J. Newman, The Impact of Elastic Deformation on Deposition Kinetics at Lithium/Polymer Interfaces, J. Electrochem. Soc. 152 (2005) A396. https://doi.org/10.1149/1.1850854.

[17] A. Parejiya, R. Amin, M.B. Dixit, R. Essehli, C.J. Jafta, D.L. Wood, I. Belharouak, Improving Contact Impedance via Electrochemical Pulses Applied to Lithium–Solid Electrolyte Interface in Solid-State Batteries, ACS Energy Lett. 6 (2021) 3669–3675. https://doi.org/10.1021/acsenergylett.1c01573.

[18] A. Parejiya, R. Amin, R. Essehli, D.L. Wood, I. Belharouak, Electrochemical Healing of Dendrites in Garnet-Based Solid Electrolytes, ACS Energy Lett. 5 (2020) 3368–3373. https://doi.org/10.1021/acsenergylett.0c01896.

[19] A. Parejiya, R. Essehli, R. Amin, J. Liu, N. Muralidharan, I. Harry M. Meyer, I. David L. Wood, I.

Belharouak, Na1+xMnx/2Zr2–x/2(PO4)3 as a Li+ and Na+ Super Ion Conductor for Solid-State Batteries, ACS Energy Lett. 6 (2021) 429–436. https://doi.org/10.1021/ACSENERGYLETT.0C02513.

[20] R. Pfenninger, M. Struzik, I. Garbayo, E. Stilp, J.L.M. Rupp, A low ride on processing temperature for fast lithium conduction in garnet solid-state battery films, Nat. Energy. 4 (2019) 475–483. https://doi.org/10.1038/s41560-019-0384-4.

[21] F. Shen, M. Dixit, X. Xiao, K. Hatzell, The Effect of Pore Connectivity on Li Dendrite Propagation Within LLZO Electrolytes Observed with Synchrotron X-ray Tomography, ACS Energy Lett. (2018) acsenergylett.8b00249. https://doi.org/10.1021/acsenergylett.8b00249.

[22] A. Sharafi, C.G. Haslam, R.D. Kerns, J. Wolfenstine, J. Sakamoto, Controlling and Correlating the Effect of Grain Size with the Mechanical and Electrochemical Properties of Li7La3Zr2O12 Solid-State Electrolyte, J. Mater. Chem. A. 5 (2017) 21491–21504. https://doi.org/10.1039/c7ta06790a.

[23] A. Sharafi, H.M. Meyer, J. Nanda, J. Wolfenstine, J. Sakamoto, Characterizing the Li-Li7La3Zr2O12interface stability and kinetics as a function of temperature and current density, J. Power Sources. 302 (2016) 135–139. https://doi.org/10.1016/j.jpowsour.2015.10.053.

[24] S. Yu, R.D. Schmidt, R. Garcia-Mendez, E. Herbert, N.J. Dudney, J.B. Wolfenstine, J. Sakamoto, D.J. Siegel, Elastic Properties of the Solid Electrolyte Li7La3Zr2O12 (LLZO), Chem. Mater. 28 (2015) 197–206.

[25] X. Han, Y. Gong, K. Fu, X. He, G.T. Hitz, J. Dai, A. Pearse, B. Liu, H. Wang, G. Rubloff, Y. Mo, V. Thangadurai, E.D. Wachsman, L. Hu, Negating interfacial impedance in garnet-based solid-state Li metal batteries, Nat. Mater. 16 (2017) 572–579. https://doi.org/10.1038/nmat4821.

[26] S. Kim, C. Jung, H. Kim, K.E. Thomas-Alyea, G. Yoon, B. Kim, M.E. Badding, Z. Song, J.M. Chang, J. Kim, D. Im, K. Kang, The Role of Interlayer Chemistry in Li-Metal Growth through a Garnet-Type

Solid Electrolyte, Adv. Energy Mater. 10 (2020) 1–11. https://doi.org/10.1002/aenm.201903993.

[27] M. Wang, J. Sakamoto, Correlating the interface resistance and surface adhesion of the Li metal-solid electrolyte interface, J. Power Sources. 377 (2018) 7–11. https://doi.org/10.1016/j.jpowsour.2017.11.078.

[28] V. Thangadurai, S. Narayanan, D. Pinzaru, Garnet-Type Solid-State Fast Li Ion Conductors for Li batteries: Critical Review, Chem. Soc. Rev. 43 (2014) 4714–4727.

[29] B.D. McCloskey, Attainable Gravimetric and Volumetric Energy Density of Li-S and Li Ion Battery Cells with Solid Separator-Protected Li Metal Anodes, J. Phys. Chem. Lett. 6 (2015) 4581–4588. https://doi.org/10.1021/acs.jpclett.5b01814.

[30] M.B. Dixit, W. Zaman, Y. Bootwala, Y. Zheng, C. Marta, Scalable manufacturing of hybrid solid electrolytes with interface control, (2019) 1–32.

[31] J. Kasemchainan, S. Zekoll, D. Spencer Jolly, Z. Ning, G.O. Hartley, J. Marrow, P.G. Bruce, Critical stripping current leads to dendrite formation on plating in lithium anode solid electrolyte cells, Nat. Mater. 18 (2019) 1105–1111. https://doi.org/10.1038/s41563-019-0438-9.

[32] D. Spencer Jolly, Z. Ning, J.E. Darnbrough, J. Kasemchainan, G.O. Hartley, P. Adamson, D.E.J. Armstrong, J. Marrow, P.G. Bruce, Sodium/Na β" Alumina Interface: Effect of Pressure on Voids, ACS Appl. Mater. Interfaces. 12 (2020) 678–685. https://doi.org/10.1021/acsami.9b17786.

[33] E. Kazyak, K.H. Chen, K.N. Wood, A.L. Davis, T. Thompson, A.R. Bielinski, A.J. Sanchez, X. Wang, C. Wang, J. Sakamoto, N.P. Dasgupta, Atomic Layer Deposition of the Solid Electrolyte Garnet Li7La3Zr2O12, Chem. Mater. 29 (2017) 3785–3792. https://doi.org/10.1021/acs.chemmater.7b00944.

[34] J. Kasemchainan, G. Peter, All-Solid-State Batteries and their Remaining Challenges, Johnson

Matthey Technol. Rev. 2 (2018) 177–180.

[35] K.B. Hatzell, M.B. Dixit, S.A. Berlinger, A.Z. Weber, Understanding Inks for Porous-Electrode Formation, J. Mater. Chem. A. 5 (2017) 20527–20533.

[36] M. Dixit, B. Harkey, F. Shen, K.B. Hatzell, Catalyst layer ink interactions that affect coatability, J. Electrochem. Soc. 165 (2018) F1-F.

[37] F. Shen, M.B. Dixit, W. Zaman, N. Hortance, B. Rogers, K.B. Hatzell, Composite Electrode Ink Formulation for All Solid-State Batteries, J. Electrochem. Soc. 166 (2019) A3182–A3188. https://doi.org/10.1149/2.0141914jes.

[38] A. Kusoglu, D. Kushner, D.K. Paul, K. Karan, M.A. Hickner, A.Z. Weber, Impact of substrate and processing on confinement of nafion thin films, Adv. Funct. Mater. 24 (2014) 4763–4774. https://doi.org/10.1002/adfm.201304311.

[39] G. V Franks, C.T. Andr, R. Studart, M.L. Sesso, S. Leo, Colloidal processing : enabling complex shaped ceramics with unique multiscale structures, J. Am. Ceram. Soc. 100 (2017) 458–490. https://doi.org/10.1111/jace.14705.

[40] D. Liu, L.-C. Chen, T.-J. Liu, T. Fan, E.-Y. Tsou, C. Tiu, An Effective Mixing for Lithium Ion Battery Slurries, Adv. Chem. Eng. Sci. 04 (2014) 515–528. https://doi.org/10.4236/aces.2014.44053.

[41] M. Schmitt, R. Diehm, P. Scharfer, W. Schabel, An experimental and analytical study on intermittent slot die coating of viscoelastic battery slurries, J. Coatings Technol. Res. 12 (2015) 927–938. https://doi.org/10.1007/s11998-015-9717-9.

[42] X. Ding, T.F. Fuller, T.A.L. Harris, A simulation model to approximate penetration of a non-Newtonian fluid into a porous media during slot die coating, J. Coatings Technol. Res. 11 (2014) 83–87. https://doi.org/10.1007/s11998-013-9501-7.

[43] J. Nam, M.S. Carvalho, Two-layer tensioned-web-over-slot die coating : Effect of die lip geometry, Chem. Eng. Sci. 65 (2010) 4014–4026. https://doi.org/10.1016/j.ces.2010.03.044.

[44] K. Bhamidipati, S. Didari, T.A.L. Harris, Experimental Study on Air Entrainment in Slot Die Coating of High-Viscosity , Shear-Thinning Fluids, Chem. Eng. Sci. 80 (2012) 195–204. https://doi.org/10.1016/j.ces.2012.06.033.

[45] T. Goda, Y. Sasaki, M. Mizuno, K. Morizawa, H. Katakura, S. Tomiya, Numerical analysis for predicting the operability window of slot- die coating onto porous media, J. Coatings Technol. Res. 14 (2017) 1053–1060. https://doi.org/10.1007/s11998-017-9985-7.

[46] S. Khandavalli, J.P. Rothstein, The e ff ect of shear-thickening on the stability of slot-die coating, (n.d.) 1–31.

[47] X. Ding, J. Liu, A Review of the Operating Limits in Slot Die Coating Processes, AIChE J. 62 (2016) 2508–2524. https://doi.org/10.1002/aic.

[48] R.H. Ottewill, Colloid Stability and Instability: “Order Disorder,” Langmuir. 5 (1989) 4–11. https://doi.org/10.1021/la00085a002.

[49] D. Grasso, K. Subramaniam, M. Butkus, K. Strevett, J. Bergendahl, A review of non-DLVO interactions in environmental colloidal systems, Rev. Environ. Sci. Biotechnol. 1 (2002) 17–38. https://doi.org/10.1023/A:1015146710500.

[50] R. Hidalgo-Álvarez, A. Martín, A. Fernández, D. Bastos, F. Martínez, F.J. De Las Nieves, Electrokinetic properties, colloidal stability and aggregation kinetics of polymer colloids, Adv. Colloid Interface Sci. 67 (1996) 1–118. https://doi.org/10.1016/0001-8686(96)00297-7.

[51] R. Rajagopalan, Stability of colloidal dispersions: A thermodynamic approach, Water Sci. Technol. 27 (1993) 117–129.

[52] W.B. Hawley, J. Li, Beneficial rheological properties of lithium-ion battery cathode slurries from elevated mixing and coating temperatures, J. Energy Storage. 26 (2019) 100994. https://doi.org/10.1016/J.EST.2019.100994.

[53] E.B. Gutoff, E.D. Cohen, G.I. Kheboian, Coating and Drying Defects Troubleshooting Operating Problems, n.d.

[54] D.L. Wood, M. Wood, J. Li, Z. Du, R.E. Ruther, K.A. Hays, N. Muralidharan, L. Geng, C. Mao, I. Belharouak, Perspectives on the relationship between materials chemistry and roll-to-roll electrode manufacturing for high-energy lithium-ion batteries, Energy Storage Mater. 29 (2020) 254–265. https://doi.org/10.1016/J.ENSM.2020.04.036.

[55] B. Bitsch, J. Dittmann, M. Schmitt, P. Scharfer, W. Schabel, N. Willenbacher, A novel slurry concept for the fabrication of lithium-ion battery electrodes with beneficial properties, J. Power Sources. 265 (2014) 81–90. https://doi.org/10.1016/j.jpowsour.2014.04.115.

[56] S. Li, K. Terao, Colloidal Dispersion of a Perfluorosulfonated Ionomer in Water–Methanol Mixtures, Polymers (Basel). 10 (2018) 72. https://doi.org/10.3390/polym10010072.

[57] S.J. Lee, T.L. Yu, H.L. Lin, W.H. Liu, C.L. Lai, Solution properties of nafion in methanol/water mixture solvent, Polymer (Guildf). 45 (2004) 2853–2862. https://doi.org/10.1016/j.polymer.2004.01.076.

[58] M. Boström, V. Deniz, G. V. Franks, B.W. Ninham, Extended DLVO theory: Electrostatic and non-electrostatic forces in oxide suspensions, Adv. Colloid Interface Sci. 123–126 (2006) 5–15. https://doi.org/10.1016/j.cis.2006.05.001.

[59] M.S. Romero-Cano, A. Martín-Rodríguez, F.J. De las Nieves, Electrosteric stabilization of polymer colloids with different functionality, Langmuir. 17 (2001) 3505–3511.

https://doi.org/10.1021/la001659l.

[60] C.M. Hansen, Hansen Solubility parameters, 2013. https://doi.org/10.1017/CBO9781107415324.004.

[61] A. Bowino, G. Capannelli, S. Munari, S. Chimico-fisici, S. Naturali, C.C. Industriale, Solubility Parameters of Poly (vinylidene fluoride), 26 (1988) 785–794.

[62] M. Dixit, K.B. Hatzell, Understanding binary interactions and aging effects in catalyst layer inks for controlled manufacturing, ECS Trans. 80 (2017) 301.

[63] V. Akbarzadeh, Coupled Fluid-Particle Modeling of a Slot Die Coating System, 62 (2016). https://doi.org/10.1002/aic.